

# Whole-Body Biodistribution and Radiation Dosimetry of $^{18}\text{F}$ -FP-(+)-DTBZ ( $^{18}\text{F}$ -AV-133): A Novel Vesicular Monoamine Transporter 2 Imaging Agent

Kun-Ju Lin<sup>\*1,2</sup>, Yi-Hsin Weng<sup>\*3</sup>, Shiao-Pyng Wey<sup>1,2</sup>, Ing-Tsung Hsiao<sup>1,2</sup>, Chin-Song Lu<sup>3</sup>, Daniel Skovronsky<sup>4</sup>, Hsiu-Ping Chang<sup>1</sup>, Mei-Ping Kung<sup>1,5</sup>, and Tzu-Chen Yen<sup>1</sup>

<sup>1</sup>Department of Nuclear Medicine and Molecular Imaging Center, Chang Gung Memorial Hospital, Taoyuan, Taiwan; <sup>2</sup>Department of Medical Imaging and Radiological Sciences, Chang Gung University, Taoyuan, Taiwan; <sup>3</sup>Department of Neurology, Chang Gung Memorial Hospital, Taoyuan, Taiwan; <sup>4</sup>Avid Radiopharmaceuticals, Inc., Philadelphia, Pennsylvania; and <sup>5</sup>Department of Radiology, University of Pennsylvania, Philadelphia, Pennsylvania

Vesicular monoamine transporter 2 (VMAT2) is highly expressed in the endocrine cells and brain. We investigated the biodistribution and radiation dosimetry of (2*R*,3*R*,11*bR*)-9-(3- $^{18}\text{F}$ -fluoropropoxy)-3-isobutyl-10-methoxy-2,3,4,6,7,11*b*-hexahydro-1*H*-pyrido[2,1-*a*]isoquinolin-2-ol ( $^{18}\text{F}$ -FP-(+)-dihydrotetrabenazine [DTBZ] or  $^{18}\text{F}$ -AV-133), a potential VMAT2 imaging agent showing encouraging results in humans, to facilitate its future clinical use. **Methods:** Nine healthy human subjects (mean age  $\pm$  SD, 58.6  $\pm$  4.2 y) were enrolled for the whole-body PET scan. Serial images were acquired for 3 h immediately after a bolus injection of 390.7  $\pm$  22.9 MBq of  $^{18}\text{F}$ -AV-133 per individual. The source organs were delineated on PET/CT images. The OLINDA/EXM application was used to determine the equivalent dose for individual organs. **Results:** The radiotracer did not show any noticeable adverse effects for the 9 subjects examined. The radioactivity uptake in the brain was the highest at 7.5%  $\pm$  0.6% injected dose at 10 min after injection. High absorbed doses were found in the pancreas, liver, and upper large intestine wall. The highest-dosed organ, which received 153.3  $\pm$  23.8  $\mu\text{Gy}/\text{MBq}$ , was the pancreas. The effective dose equivalent and effective dose for  $^{18}\text{F}$ -AV-133 were 36.5  $\pm$  2.8 and 27.8  $\pm$  2.5  $\mu\text{Sv}/\text{MBq}$ , respectively. These values are comparable to those reported for any other  $^{18}\text{F}$ -labeled radiopharmaceutical. **Conclusion:**  $^{18}\text{F}$ -AV-133 is safe, with appropriate biodistribution and radiation dosimetry for imaging VMAT2 sites in humans.

**Key Words:** vesicular monoamine transporter 2; whole-body biodistribution; dosimetry; PET; Parkinson disease

**J Nucl Med 2010; 51:1480–1485**

DOI: 10.2967/jnumed.110.078196

Received Apr. 23, 2010; revision accepted Jun. 10, 2010.

For correspondence or reprints contact: Tzu-Chen Yen, Department of Nuclear Medicine and Molecular Imaging Center, Chang Gung Memorial Hospital, 5. Fu-Hsing St., Kwei Shan Hsiang, Taoyuan, Taiwan.

E-mail: yen1110@adm.cgmh.org.tw

\*Contributed equally to this work.

COPYRIGHT © 2010 by the Society of Nuclear Medicine, Inc.

Vesicular monoamine transporter type 2 (VMAT2) is an integral part of the reuptake mechanism for vesicular packaging and storage of monoamine neurotransmitters in the synapses of the brain. Imaging VMAT2 in the brain thus provides a measurement reflecting the integrity (total number) of all 3 monoaminergic neurons (1,2). Parkinson disease (PD) involves degeneration of nigrostriatal neurons with a prominent dopaminergic terminal loss in the striatum. A plethora of dopamine transporter imaging agents, most of which are tropane (or cocaine) derivatives with varying degrees of affinities to serotonin and norepinephrine transporters, have been reported as useful tools for the diagnosis of PD (3–7). One study (3) pointed out the deficiencies in imaging PD based on dopamine transporter tracers, which highlighted the need for additional new imaging agents to reliably diagnose and predict the progress of this neurodegenerative disease. Imaging of the VMAT2 has thus been proposed as an alternative for following degeneration of monoaminergic neurons in PD (8).  $^{11}\text{C}$ -tetrabenazine and derivatives targeting VMAT2 have been successfully developed and tested in humans (9). Animal data showed that  $^{11}\text{C}$ -(+)-dihydrotetrabenazine (DTBZ) is less sensitive to drugs affecting dopamine levels in the brain; therefore, it will more accurately reflect the concentration of viable monoamine neurons (10–13). Rapid and differential losses of in vivo dopamine transporter and VMAT2 radioligand binding in mice treated with 1-methyl-4-phenyl-1,2,3,6-tetrahydropyridine were detected by  $^3\text{H}$ -( $\pm$ )-DTBZ, suggesting that the VMAT2 binding sites are proportionally related to the existence of functional dopamine neurons (13,14). Thus,  $^{11}\text{C}$ -(+)-DTBZ could be a potentially useful marker for VMAT2 reduction. The reduction of VMAT2 directly reflects the loss of monoamine neurons; therefore, it is applicable as a tool in the diagnosis of PD (8).

To meet a similar goal with a wider application, an  $^{18}\text{F}$ -labeled analog of DTBZ ( $^{18}\text{F}$ -AV-133) (Supplemental Fig. 1; supplemental materials are available online only at <http://jnm.snmjournals.org>) with a longer physical half-life ( $T_{1/2}$ ) of 110 min (vs. 20 min for  $^{11}\text{C}$ ) has been recently developed (15).  $^{18}\text{F}$ -AV-133 displayed an excellent binding affinity ( $K_i = 0.11$  nM, rat striatal homogenates) for VMAT2 (15,16). Successful imaging studies in rodents and monkeys using  $^{18}\text{F}$ -AV-133 have been reported (17). An initial trial to assess the reduction of VMAT2 binding sites in patients with PD and dementia with Lewy bodies was performed by Koeppe et al. (18) and Suzuki et al. (19). A recent publication clearly indicated the sensitivity of  $^{18}\text{F}$ -AV-133 for detecting monoaminergic terminal reductions in PD patients and concluded that  $^{18}\text{F}$ -AV-133 may allow the selection of presymptomatic patients with nigrostriatal movement disorders (20).

In the present study, we analyzed in detail the biodistribution, dosimetry, and safety data for  $^{18}\text{F}$ -AV-133 in humans. With these data, future studies can be expanded into the clinical setting to test the usefulness of  $^{18}\text{F}$ -AV-133 in the diagnosis and monitoring of PD and related movement disorders.

## MATERIALS AND METHODS

### Preparation of $^{18}\text{F}$ -AV-133

Optically pure  $^{18}\text{F}$ -AV-133 was synthesized at the cyclotron facility of Chang Gung Memorial Hospital following the method described previously, with some modification (16). The radiochemical purity of  $^{18}\text{F}$ -AV-133 determined by analytic high-performance liquid chromatography was greater than 98%, and the specific activity was 60–200 TBq/mmol at the end of synthesis.

### Subjects

Nine healthy elderly controls (6 men and 3 women; mean age  $\pm$  SD,  $58.6 \pm 4.2$  y) were enrolled for the study, and none had a history of physical or neurologic illnesses. Results of laboratory investigations were in the reference range for all controls. The study protocol was approved by the Institutional Review Board of the Chang Gung Memorial Hospital and the Governmental Department of Health. Details on the imaging protocol and the main characteristics of the study participants are shown in Table 1.

### PET/CT

Whole-body (WB) PET was used to characterize the biodistribution of  $^{18}\text{F}$ -AV-133. Serial WB scans were acquired on a Discovery ST16 PET/CT scanner (GE Healthcare) for all subjects. The details of image acquisition and processing have been described by our group (21). In brief, serial WB PET images were acquired in 3 scanning sessions after the intravenous injection of  $^{18}\text{F}$ -AV-133 ( $390.8 \pm 22.9.0$  MBq). Each PET scan session consisted of 2 consecutive 20-min scans. Subjects were permitted to leave the scanner and void freely during each 10- to 20-min break between successive scan sessions. Urine samples were collected, and total urinary radioactivity was determined. An additional 10-min 3-dimensional PET brain image was acquired before WB image session 3, starting at 110 min after injection (Fig. 1). The WB images, with resolutions of  $4.69 \times 4.69 \times 3.27$  mm (matrix size,  $128 \times 128$ ; 299 slices), were reconstructed using 2-dimensional ordered-subsets expectation maximization with 4 iterations, 15 subsets, gaussian filtering of 5.14 mm, and zoom of 1. Brain PET images were reconstructed using 3-dimensional ordered-subsets expectation maximization (subsets, 16; iterations, 4; gaussian filter, 2.98 mm; and zoom of 2). All PET images were attenuation-corrected with low-dose helical CT.

The uptake of  $^{18}\text{F}$ -AV-133 in the target organs was determined by calculation of the standardized uptake value (SUV) according to the following formula:

$$\text{SUV} = \frac{\text{Decay corrected tissue activity (Bq/mL)}}{\text{Injected dose (Bq)/body weight (g)}} \quad \text{Eq. 1}$$

Mean SUVs of the organs of interest determined at time  $t$  after injection  $\overline{\text{SUV}}_{\text{organ}}(t)$  were assessed in all patients.

### Dosimetry

The OLINDA/EXM application (version 1.0) developed by Stabin et al. (Vanderbilt University) (22) was used to determine the effective doses and doses to individual organs on calculations and constants defined in the ICRP Publication 60 (23) for all subjects. The dynamic bladder model and the gastrointestinal tract model (defined in ICRP 30) were used (24–26). The residence time ( $\tau_h$ ) for each organ (h) was determined for dose estimation (25).

The details of image processing for dose estimation have been described by our group (21). In brief, volumes of interest were drawn on fused serial PET/CT images for the following organs: brain, thyroid, lungs, heart, liver, gallbladder, pancreas, kidneys, stomach, spleen, urinary bladder, intestine, lumbar spines, and

**TABLE 1.** Injection Dose, Specific Activity at Time of Delivery, and General Characteristics of Study Participants

Patient no.	Injection dose (MBq)	Specific activity (TBq/mmol)	Sex	Age (y)	Body weight (kg)
1	409.8	8.9	M	60	65
2	353.4	14.2	M	60	82
3	384.2	14.2	M	56	78
4	430.5	11.0	M	56	74
5	401.2	23.2	F	58	81
6	403.0	15.4	M	60	65
7	384.4	10.5	M	64	70
8	377.8	24.9	F	63	64
9	372.5	14.4	F	50	52

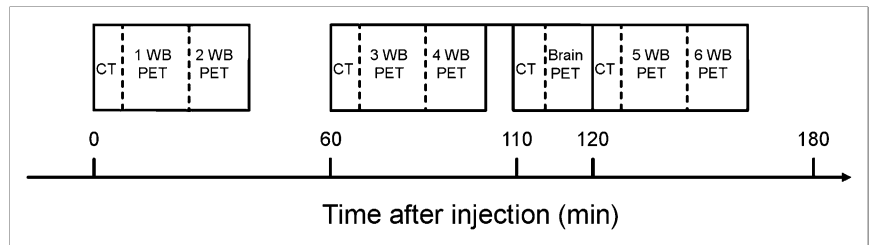


**FIGURE 1.** Acquisition scheme for biodistribution study.

testes. Because the lumbar vertebrae contain approximately 12.3% of the red marrow in the adult, this source organ was used as an approximation for uptake in the red marrow (27). At each time point, we assessed the percentage of injected  $^{18}\text{F}$ -AV-133 (percentage injected dose [%ID]) within all volumes of interest according to the following formula:

$$\%ID(t) = 100\% \times \overline{\text{SUV}}_{\text{organ}}(t) \times \frac{V_{\text{organ}}}{M_{\text{whole body}}}, \quad \text{Eq. 2}$$

where %ID( $t$ ),  $V_{\text{organ}}$ , and  $M_{\text{whole body}}$  are the %ID measured at time  $t$  after injection, the volume of the organ ( $\text{cm}^3$ ), and the mass of the WB (g), respectively. In general, the measured kinetic data (with the exclusion of the urinary bladder and intestine) can be represented as one or more exponential terms of a mathematic expression, as follows:

$$\text{Activity}(t) = A \times \exp(-a \times t) + B \times \exp(-b \times t) + C \times \exp(-c \times t), \quad \text{Eq. 3}$$

where  $A$ ,  $B$ , and  $C$  are initial activities or concentrations, and  $a$ ,  $b$ , and  $c$  are decay or removal rate constants. This mathematic model—Activity( $t$ )—was fitted to the measured kinetic data—%ID( $t$ )—by least-squares analysis using the EXM module in the OLINDA/EXM application. Then, the  $\tau_h$  of each organ was calculated on the basis of the physical  $T_{1/2}$  of the radioisotope and the integral of the fitted time–activity curve from time zero to infinity, as follows:

$$\int_0^{\infty} \text{Activity}(t) dt = \frac{A}{a} + \frac{B}{b} + \frac{C}{c}. \quad \text{Eq. 4}$$

The  $\tau_h$  values were entered into the OLINDA kinetics input form to be used for dose calculations (22).

For a conservative estimation of gastrointestinal kinetics data, decay-corrected peak activity in the entire abdomen—excluding the liver, gallbladder, pancreas, and kidneys—was used as the input to the small intestine in the ICRP 30 gastrointestinal tract model (26). The fraction of activity excreted through the bladder and the corresponding biologic  $T_{1/2}$  were assessed from the accumulated activity excreted at all voiding moments between and after scans (at  $\sim 1$ , 2, and 3 h after injection). The amount of urinary radioactivity at 10 and 30 min after injection was determined from WB scans. The 1-phase exponential association curve was then fitted to the cumulative urine activity using the following formula:

$$U(t) = U_{\text{max}} \times (1 - \exp(-\ln 2 \times t/T_{1/2})), \quad \text{Eq. 5}$$

where  $U(t)$ ,  $U_{\text{max}}$ , and  $T_{1/2}$  are the accumulated urine fraction at time  $t$ , maximum accumulated urine collected, and biologic  $T_{1/2}$ , respectively. To assess the  $\tau_h$  for the urinary bladder content, these parameters were entered into the bladder-voiding model module of OLINDA/EXM, with voiding intervals of 2.4 and 4.8 h. Dose estimates for different organs were made with the MIRD algorithm (25) by entering the kinetic data into the OLINDA/EXM application. The  $\tau_h$  values in the rest of the body were obtained by subtracting the total organ  $\tau_h$  values from the theoretic total body  $\tau_h$  computed from the half-life ( $T_{1/2}/\ln 2 = 2.62$ ).

## RESULTS

### Subject Characteristics

Vital signs and electrocardiogram recordings were obtained before injection of the radiotracer, in the resting

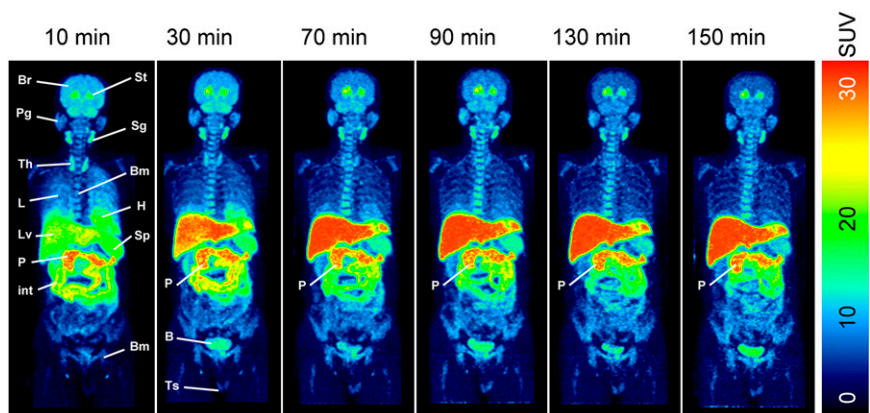


**FIGURE 2.** Coronal projections (75-mm thick) of 6 sequential WB PET images taken at 10, 30, 70, 90, 130, and 150 min after injection of  $^{18}\text{F}$ -AV-133 in 1 subject. Images are displayed on SUV scale. B = bladder; Bm = bone marrow; Br = brain; H = heart; int = intestine; L = lung; Lv = liver; P = pancreas; Pg = parotid gland; Sg = submandibular gland; Sp = spleen; St = straitum; Th = thyroid; Ts = testes.

periods between the scans, and at the end of the study. There were no consistent, significant changes in vital signs and electrocardiogram readings. No serious adverse events were observed.

### **<sup>18</sup>F-AV-133 Biodistribution**

WB images of <sup>18</sup>F-AV-133 biodistribution at various intervals are shown in Figure 2. The liver and pancreas were visually identified as the organs containing the highest concentration of radioactivity. Accumulation of radioactivity was observed within the intestine at later times. A moderate uptake of <sup>18</sup>F-AV-133 was observed in the kidneys, urinary bladder, bone marrow, and brain (Fig. 2). The <sup>18</sup>F-AV-133 biodistribution in the brain, kidneys, heart, liver, lungs, pancreas, spleen, and urinary bladder is shown in Supplemental Figure 2. The time–activity curve showed a high initial uptake of the radiotracer in the liver and brain, with values of  $16.36 \pm 3.11$  and  $7.48 \pm 0.58$  %ID, respectively. The radioactivity declined in most organs at the end of the study (i.e., at 3 h after injection), except the liver, pancreas, and urinary bladder. The urine excretion of the 9 subjects is shown in Supplemental Figure 2H. This analysis yielded a  $U_{\max}$  value of  $3.46 \pm 0.99$  %ID and a biologic  $T_{1/2}$  of  $0.88 \pm 0.44$  h.

The  $\tau_h$  values of source organs are listed in Table 2. The <sup>18</sup>F-AV-133 radiation doses for a 73.7-kg adult phantom are calculated and shown in Supplemental Table 1. Considering a voiding interval of 2.4 h, the highest absorbed organ doses were to the pancreas ( $153.3 \pm 23.8$   $\mu$ Gy/MBq), liver ( $72.0 \pm 13.6$   $\mu$ Gy/MBq), and upper large intestine ( $54.5 \pm 9.2$

$\mu$ Gy/MBq). A high variability in estimated radiation doses was found in the thyroid, lungs, and stomach wall, and this was most likely due to the physical and functional clearance rates within these organs. The mean effective dose in adult was  $27.8 \pm 2.5$   $\mu$ Sv/MBq. A more conservative dose calculation of  $28.6 \pm 2.3$   $\mu$ Sv/MBq was listed with a urinary interval of 4.8 h (Supplemental Table 1). This value is comparable to values from other PET tracers for clinical routine use (28,29) and makes <sup>18</sup>F-AV-133 suitable for clinical imaging applications, including longitudinal studies.

Figure 3 shows the transverse brain images of a representative healthy subject at the level of the striatum, caudate head, and brain stem. The images were acquired between 110 and 120 min after tracer injection. A prominent uptake of radioactivity in the caudate, putamen, substantia nigra, hippocampus, and brain stem regions was clearly delineated, and these regions correspond well to the distribution pattern of VMAT2 in the brain.

### **DISCUSSION**

The biodistribution study of <sup>18</sup>F-AV-133 in humans showed a high initial ( $16.4 \pm 3.1$  %ID) and maximum ( $22.0 \pm 5.0$  %ID) uptake of radioactivity in the liver, indicating that the elimination of <sup>18</sup>F-AV-133 is mainly through the hepatobiliary system. The prominent liver uptake of <sup>18</sup>F-AV-133 was similar to that observed for its structural analog tetrabenazine pharmacokinetics demonstrated by previous human (30,31) and primate (32) studies. The distribution of radioactive material in the liver is probably due

**TABLE 2.** Descending Order of Average Number of Disintegrations in Source Organs

Source organ	Mean	SD	Percentage coefficient of variation
Remainder	1.08E+00	1.57E−01	14.6
Liver	5.41E−01	1.13E−01	20.8
Red marrow*	2.72E−01	4.71E−02	17.3
Small intestine	1.79E−01	3.74E−02	20.9
Brain	1.28E−01	2.36E−02	18.4
Lungs	1.08E−01	5.23E−02	48.3
Upper large intestine	9.82E−02	2.05E−02	20.9
Pancreas	7.78E−02	1.30E−02	16.8
Urinary bladder contents at 4.8 h <sup>†</sup>	4.78E−02	1.46E−02	30.5
Stomach	3.62E−02	1.96E−02	54.2
Kidneys	3.19E−02	1.03E−02	32.4
Urinary bladder contents at 2.4 h <sup>†</sup>	2.93E−02	9.35E−03	31.9
Spleen	2.46E−02	5.45E−03	22.2
Heart wall	2.42E−02	5.20E−03	21.6
Lower large intestine	1.80E−02	3.77E−03	21.0
Gallbladder contents	8.35E−03	3.04E−03	36.4
Thyroid	4.75E−03	2.69E−03	56.6
Testes <sup>‡</sup>	4.40E−03	1.44E−03	32.8

\*Data are scaled from lumbar vertebrae.

<sup>†</sup>2.4 and 4.8 h are voiding intervals.

<sup>‡</sup>Data are based on 6 male subjects.

Data for average number of disintegrations in source organs (i.e., residence time) are in MBq-h/MBq. Percentage coefficient of variation is determined by  $SD/mean \times 100\%$ .

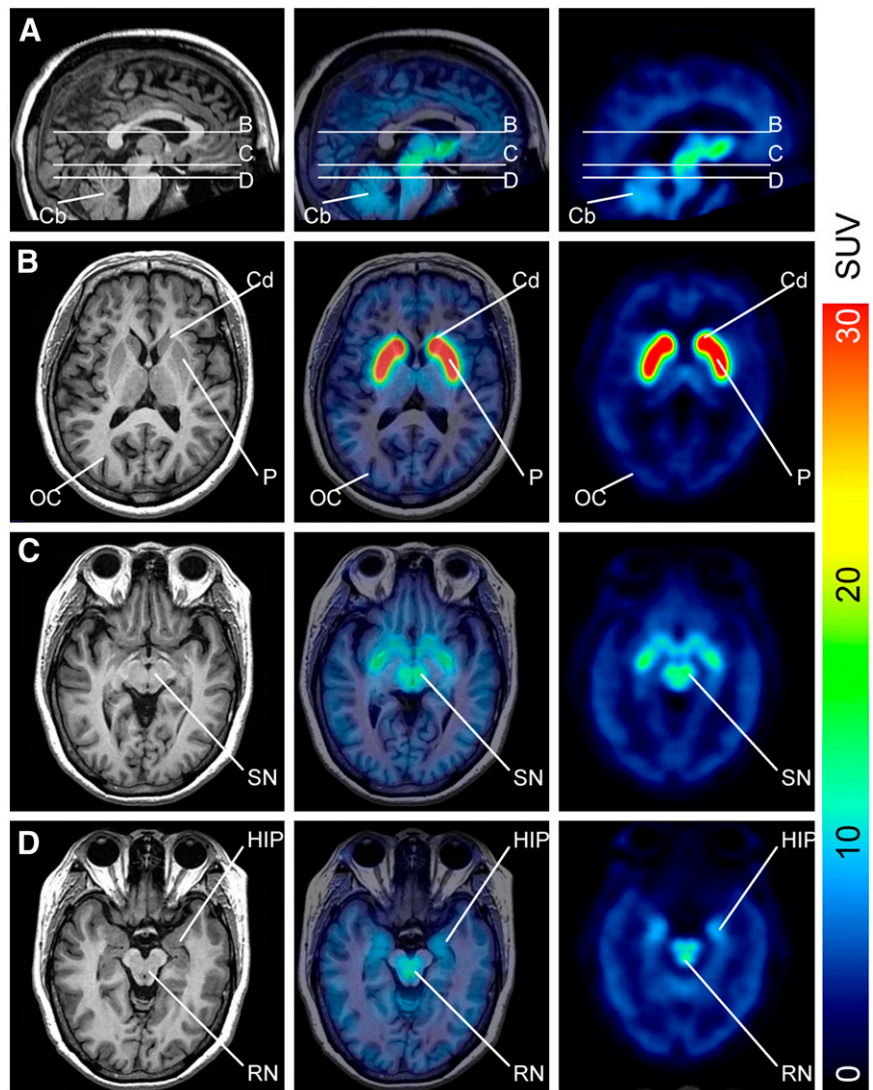


**FIGURE 3.** MR image, MR and  $^{18}\text{F}$ -AV-133 PET fusion image, and  $^{18}\text{F}$ -AV-133 PET image of healthy 56-y-old man at level of striatum (B), caudate head (C), and brain stem (D). These 3 levels are shown in panel A. Images were acquired between 110 and 120 min after injection. Cb = cerebellum; Cd = caudate; HIP = hippocampus; OC = occipital cortex; P = putamen; RN = raphi nucleus; SN = substantia nigra.

to hepatic dealkylation of  $^{18}\text{F}$ -AV-133, as reported previously for  $^{11}\text{C}$ -DTBZ (30,31). The high liver uptake in humans is consistent with the reported high values of 3.53 %ID/g in rat (33) and 24.6 %ID/g in mouse (16) studies. However, the hepatic clearance of radioactivity is slow, and only a small amount reaches the gallbladder up to 3 h after intravenous injection of  $^{18}\text{F}$ -AV-133 in humans. In contrast, the radioactivity clearance is much faster in the small-animal studies. Species differences could be a factor.

In parallel to the animal biodistribution results (33),  $^{18}\text{F}$ -AV-133 was prominently distributed in the pancreas immediately after tracer injection. The radioactivity distribution in the pancreas reached its peak and ranked as the highest image intensity among all organs within the first hour after injection. Past an hour after tracer injection, high image contrast for delineating the pancreas was clearly achieved when the radioactivity distribution in the muscle, intestine, and kidneys was low. It is suggested that  $^{18}\text{F}$ -AV-133 distribution in the pancreas is related to the VMAT2 expressed within the  $\beta$ -cells of the pancreatic islet (34). According to

the binding study with  $^{18}\text{F}$ -AV-133 using human islet homogenates and in vitro autoradiography, a specific VMAT2 binding signal can be clearly detected (35). Together with our biodistribution findings, the potential role for this VMAT2 ligand to evaluate  $\beta$ -cell function warrants further study.

The moderate uptake and fast decline of  $^{18}\text{F}$ -AV-133 in the lung was noted. Radioactivity clearance is relatively longer from the lung than from blood-containing organs such as heart or spleen. According to a previous report, radiolabeled methanol may be one of the metabolites for  $^{11}\text{C}$ -DTBZ (31). The metabolites of  $^{18}\text{F}$ -AV-133 have not been fully characterized. However, it is possible, judging from its structure, that  $^{18}\text{F}$ -propanol is a candidate metabolite. In this regard, the radioactivity in the lung may be due to exhalation of radioactive metabolites after the hepatic dealkylation process. Activity observed in the lungs may also be located in the endocrine component of the sympathetic and parasympathetic nervous systems (36).

As expected, VMAT2 is a general histochemical marker for biogenic amine-containing neurons of the central

nervous system (36). In parallel to the biodistribution study,  $^{18}\text{F}$ -AV-133 uptake with the administered clinical dose can be found in the striatum, brain stem, hippocampus, and substantia nigra on brain images acquired at 110 min after injection (Fig. 3). These brain regions have been recognized as being related to dopamine- (nigrostriatal pathway) and serotonin (hippocampus and brain stem)-secreting neurons (35). A recent publication demonstrated the ability to differentiate healthy controls from PD subjects using  $^{18}\text{F}$ -AV-133 targeting VMAT2 (20). In addition, because uptake of  $^{18}\text{F}$ -AV-133 in the brain was not restricted to the nigrostriatal system, possible applications for studying the serotonin system relating to psychiatric disorders is also warranted.

## CONCLUSION

This study showed that  $^{18}\text{F}$ -AV-133 is a safe PET tracer for studying VMAT2 in the brain and possibly in the pancreas. The peripheral distribution of  $^{18}\text{F}$ -AV-133 was concentrated mostly in the pancreas and liver. The radiotracer was excreted mainly through the hepatobiliary system. At the clinically practical administered activity (370 MBq), the effective dose from  $^{18}\text{F}$ -AV-133 was 10.6 mSv, with a 4.8-h voiding interval.

## ACKNOWLEDGMENTS

We thank Avid Radiopharmaceuticals, Inc. (Philadelphia, PA), for providing the precursor for the preparation of  $^{18}\text{F}$ -AV-133. We are grateful to Shu-Fei Hsu, Chuan-Wei Lo, and Cheng Hsiang Yao for their excellent technical assistance. This study was carried out with financial support from the National Science Council, Taiwan (grant NSC-98-2314-B-182-034-MY2).

## REFERENCES

- Albin R, Koeppe R. Rapid loss of striatal VMAT2 binding associated with onset of Lewy body dementia. *Mov Disord.* 2006;21:287–288.
- Kilbourn MR. In vivo radiotracers for vesicular neurotransmitter transporters. *Nucl Med Biol.* 1997;24:615–619.
- Ravina B, Eidelberg D, Ahlskog JE, et al. The role of radiotracer imaging in Parkinson disease. *Neurology.* 2005;64:208–215.
- Van Laere K, Casteels C, De CL, et al. Dual-tracer dopamine transporter and perfusion SPECT in differential diagnosis of parkinsonism using template-based discriminant analysis. *J Nucl Med.* 2006;47:384–392.
- Mozley PD, Schneider JS, Acton PD, et al. Binding of [ $^{99\text{m}}\text{Tc}$ ]TRODAT-1 to dopamine transporters in patients with Parkinson's disease and in healthy volunteers. *J Nucl Med.* 2000;41:584–589.
- Stoessl AJ, de LF-F. Dopamine receptors in Parkinson's disease: imaging studies. *Adv Neurol.* 2003;91:65–71.
- Frey KA, Koeppe RA, Kilbourn MR. Imaging the vesicular monoamine transporter. *Adv Neurol.* 2001;86:237–247.
- Frey KA, Koeppe RA, Kilbourn MR, et al. Presynaptic monoaminergic vesicles in Parkinson's disease and normal aging. *Ann Neurol.* 1996;40:873–884.
- Albin RL, Koeppe RA, Bohnen NI, et al. Increased ventral striatal monoaminergic innervation in Tourette syndrome. *Neurology.* 2003;61:310–315.
- Bohnen NI, Albin RL, Koeppe RA, et al. Positron emission tomography of monoaminergic vesicular binding in aging and Parkinson disease. *J Cereb Blood Flow Metab.* 2006;26:1198–1212.
- Frey KA. Can SPET imaging of dopamine uptake sites replace PET imaging in Parkinson's disease? *Eur J Nucl Med Mol Imaging.* 2002;29:715–717.
- Lee CS, Schulzer M, de la Fuente-Fernández R, et al. Lack of regional selectivity during the progression of Parkinson disease: implications for pathogenesis. *Arch Neurol.* 2004;61:1920–1925.
- Kilbourn MR, Frey KA, Vander BT, Sherman PS. Effects of dopaminergic drug treatments on in vivo radioligand binding to brain vesicular monoamine transporters. *Nucl Med Biol.* 1996;23:467–471.
- Kilbourn MR, Kuszpit K, Sherman P. Rapid and differential losses of in vivo dopamine transporter (DAT) and vesicular monoamine transporter (VMAT2) radioligand binding in MPTP-treated mice. *Synapse.* 2000;35:250–255.
- Goswami R, Ponde DE, Kung MP, Hou C, Kilbourn MR, Kung HF. Fluoroalkyl derivatives of dihydrotetabenazine as positron emission tomography imaging agents targeting vesicular monoamine transporters. *Nucl Med Biol.* 2006;33:685–694.
- Kung MP, Hou C, Goswami R, Ponde DE, Kilbourn MR, Kung HF. Characterization of optically resolved 9-fluoropropyl-dihydrotetabenazine as a potential PET imaging agent targeting vesicular monoamine transporters. *Nucl Med Biol.* 2007;34:239–246.
- Kilbourn MR, Hockley B, Lee L, et al. Pharmacokinetics of [ $^{18}\text{F}$ ]fluoroalkyl derivatives of dihydrotetabenazine in rat and monkey brain. *Nucl Med Biol.* 2007;34:233–237.
- Koeppe RA, Gilman S, Junck L, Wernette K, Frey KA. Differentiating Alzheimer's disease from dementia with Lewy bodies and Parkinson's disease with (+)-[ $^{11}\text{C}$ ]dihydrotetabenazine positron emission tomography. *Alzheimers Dement.* 2008;4(1, suppl 1):S67–S76.
- Suzuki M, Desmond TJ, Albin RL, Frey KA. Striatal monoaminergic terminals in Lewy body and Alzheimer's dementias. *Ann Neurol.* 2002;51:767–771.
- Okamura N, Villemagne VL, Drago J, et al. In vivo measurement of vesicular monoamine transporter type 2 density in Parkinson disease with  $^{18}\text{F}$ -AV-133. *J Nucl Med.* 2010;51:223–228.
- Lin KJ, Hsu WC, Hsiao IT, et al. Whole-body biodistribution and brain PET imaging with [ $^{18}\text{F}$ ]AV-45, a novel amyloid imaging agent: a pilot study. *Nucl Med Biol.* 2010;37:497–508.
- Stabin MG, Sparks RB, Crowe E. OLINDA/EXM: the second-generation personal computer software for internal dose assessment in nuclear medicine. *J Nucl Med.* 2005;46:1023–1027.
- International Commission on Radiological Protection (ICRP). *1990 Recommendations of the International Commission on Radiological Protection.* ICRP Publication 60. New York, NY: Pergamon Press; 1991.
- Lin KJ, Liu CY, Wey SP, et al. Brain SPECT imaging and whole-body biodistribution with [ $^{123}\text{I}$ ]A. *Nucl Med Biol.* 2006;33:193–202.
- Loevinger R, Budinger T, Watson E. *MIRD Primer for Absorbed Dose Calculations.* New York, NY: The Society of Nuclear Medicine; 1988.
- International Commission on Radiological Protection (ICRP). *Part 1: Limits for Intakes of Radionuclides by Workers.* ICRP Publication 30. Oxford, U.K.: Pergamon Press; 1979.
- Valentin J. *Basic Anatomical and Physiological Data for Use in Radiological Protection: Reference Values.* ICRP Publication 89. Oxford, U.K.: Pergamon Press; 2001.
- Mejia AA, Nakamura T, Itoh M, et al. Absorbed dose estimates in positron emission tomography studies based on the administration of  $^{18}\text{F}$ -labeled radiopharmaceuticals. *J Radiat Res (Tokyo).* 1991;32:243–261.
- Meyer GJ, Waters SL, Coenen HH, Luxen A, Maziere B, Langstrom B. PET radiopharmaceuticals in Europe: current use and data relevant for the formulation of summaries of product characteristics (SPCs). *Eur J Nucl Med.* 1995;22:1420–1432.
- Roberts MS, McLean S, Millingen KS, Galloway HM. The pharmacokinetics of tetraabenazine and its hydroxy metabolite in patients treated for involuntary movement disorders. *Eur J Clin Pharmacol.* 1986;29:703–708.
- Mehvar R, Jamali F, Watson MW, Skelton D. Pharmacokinetics of tetraabenazine and its major metabolite in man and rat: bioavailability and dose dependency studies. *Drug Metab Dispos.* 1987;15:250–255.
- Murthy R, Harris P, Simpson N, et al. Whole body [ $^{11}\text{C}$ ]dihydrotetabenazine imaging of baboons: biodistribution and human radiation dosimetry estimates. *Eur J Nucl Med Mol Imaging.* 2008;35:790–797.
- Kung MP, Hou C, Lieberman BP, et al. In vivo imaging of beta-cell mass in rats using  $^{18}\text{F}$ -FP-(+)-DTBZ: a potential PET ligand for studying diabetes mellitus. *J Nucl Med.* 2008;49:1171–1176.
- Anlauf M, Eissele R, Schafer MK, et al. Expression of the two isoforms of the vesicular monoamine transporter (VMAT1 and VMAT2) in the endocrine pancreas and pancreatic endocrine tumors. *J Histochem Cytochem.* 2003;51:1027–1040.
- Tsao HH, Lin KJ, Juang JH, et al. Binding characteristics of 9-fluoropropyl-(+)-dihydrotetabenazine (AV-133) to the vesicular monoamine transporter type 2 in rats. *Nucl Med Biol.* 2010;37:413–419.
- Weithe E, Eiden LE. Chemical neuroanatomy of the vesicular amine transporters. *FASEB J.* 2000;14:2435–2449.